The Astronomical Journal, 124:3305–3312, 2002 December

ANALYSIS AND MODELS OF PHOTOIONIZED STRUCTURES SEEN IN *HUBBLE SPACE TELESCOPE* IMAGES OF NGC 7635[1]

Brian D. Moore
Department of Physics and Astronomy, Rice University, Houston, TX 77005-1892

J. Jeff Hester and Paul A. Scowen
Department of Physics and Astronomy, Arizona State University, Tempe, AZ 85287-1504

and

Donald K. Walter
Department of Physical Sciences, South Carolina State University, Orangeburg, SC 29117-7296
Received 2002 March 10; accepted 2002 September 4

ABSTRACT

We present the analysis of photoionized structures seen in *Hubble Space Telescope* Wide Field Planetary Camera 2 images of NGC 7635 and the surrounding H II region S162. We exploit the high spatial resolution images to make a census of the total ionizing flux from the O6.5 IIIf star BD +60°2522. We also construct detailed models of two structures with a photoionization code, reproducing the line emission seen in spatial profiles extracted directly from the images. We demonstrate that the density distribution of the models produces deviations in the spectrally derived elemental abundances at a level exceeding typical observational errors. Our results also show a large discrepancy between the star's effective temperature used for our best-fit models (34,320 K) and that expected based on its spectral type (>40,000 K) from a hot-star calibration taken from the literature. We suggest that this is due to the use of plane-parallel stellar atmospheres in constructing that calibration.

Key words: H II regions — ISM: individual (NGC 7635) — ISM: kinematics and dynamics — stars: individual (BD +60°2522) — stars: mass loss

1. INTRODUCTION

NGC 7635 and the surrounding H II region S162 are areas of dense material ionized by the O6.5 IIIf star BD +60°2522. We have obtained narrowband images of the northern portion of NGC 7635 with the Wide Field Planetary Camera 2 (WFPC2) and Space Telescope Imaging Spectrograph (STIS) aboard the *Hubble Space Telescope*. In this paper, we present a slightly atypical analysis of the object, with the goal of examining the physical conditions within the region, as well as that of the ionizing star itself. The reduced and calibrated data are presented in Moore et al. (2002b, hereafter Paper I), and all extractions presented herein were performed on the mosaicked frames discussed in that paper. The diffraction-limited images produced by WFPC2 afford a view of the spatially resolved ionization structure within the nebula. Section 2 presents the method used to estimate the ionizing flux incident on an emission-line region, which is then applied to NGC 7635 in § 3. Two of the ionized structures are directly modeled with a photoionization code in § 4, and the implications for the standard techniques of nebular spectral analysis are discussed. The implications of these results for the nature of the central star are discussed in § 5.

2. ESTIMATING IONIZING FLUX FROM IMAGERY

The traditional method of estimating the gas density within an ionized region is to infer it from the behavior of density-sensitive line ratios in its spectra. With a few simplifying assumptions, the density in an ionized structure can alternatively be estimated from its Hα surface brightness and geometry. In some cases the incident hydrogen-ionizing flux can also be inferred. We use this approach to investigate the structures seen in our images of NGC 7635. A brief discussion of this approach is instructive.

Consider a column of gas with constant density and temperature along a line-of-sight distance l. The observed surface brightness of this column at wavelength λ is

$$\mathrm{SB}(\lambda) = j(\lambda) l \times 10^{-C(\lambda)} , \qquad (1)$$

where $j(\lambda)$ is the volume emissivity of the gas and $C(\lambda)$ is the logarithmic reddening along the line of sight. An estimate for l can be derived from the geometry of the emitting region. For a fully ionized ellipsoidal knot, the line-of-sight distance down its center can be estimated as the geometric mean of its major and minor axes. For a thin ionized arc on the outer portion of a curved neutral knot, l at its brightest point can be estimated as the length of the chord bisected by the brightest part of the knot.

Because it constitutes the overwhelming fraction of nebular gas, hydrogen provides the best estimate of the gas density via this method. In photoionized nebulae the optical lines arise almost exclusively from recombination; the fraction of neutral hydrogen is small, and typical electron temperatures are well below the threshold to produce the excited states of H^0 in quantity. Brocklehurst (1971) calculated the hydrogen recombination spectrum over a broad

[1] Based on observations made with the NASA/ESA *Hubble Space Telescope*, obtained at the Space Telescope Science Institute (STScI), which is operated by the Association of Universities for Research in Astronomy (AURA), Inc., under NASA contract NAS 5-26555.

range of densities and temperatures. For our purposes we use the results for case B recombination, which ignores the effects of direct recombinations to the ground state. This is predicated on the assumption that the photons produced by this recombination ionize a nearby neutral atom, producing no net change in the ionized gas. Aller (1984) interpolates over the Brocklehurst results to produce an expression for the case B Hβ volume emissivity; combined with $j(\mathrm{H}\alpha)/j(\mathrm{H}\beta) = 2.847$ for $n_e = 10^4$ cm^{-3} and $T_e = 10^4$ K (also from Brocklehurst), the Hα volume emissivity is

$$j(\mathrm{H}\alpha) = 3.14 \times 10^{-26} n_p n_e f(t_4) \text{ ergs cm}^{-3} \text{ s}^{-1} \text{ sr}^{-1} , \quad (2)$$

where $t_4 = T_e/(10^4 \text{ K})$ and $f(t_4) = t^{-0.983} 10^{-0.0424/t}$. This expression is accurate to 10% under the range of physical conditions expected in photoionized nebulae. The value of $C(\mathrm{H}\alpha)$ can be derived from an assumed reddening law and the deviation of Hα/Hβ from the expected value. If we assume an He/H ratio of 0.1 by number and that He^+ is its dominant species, then $n_e \simeq 1.1 n_p$. Thus, the hydrogen density within a given structure can be estimated as

$$n_p^2 = 9.4 \times 10^6 \frac{\mathrm{SB}(\mathrm{H}\alpha)}{f(t_4) l(\mathrm{pc})} 10^{C(\mathrm{H}\alpha)} , \quad (3)$$

where SB(Hα) is in ergs cm^{-2} s^{-1} sr^{-1}. Even with the number of simplifications employed in this derivations, the dominant uncertainty will be from the estimate of l.

This line of reasoning can be continued to produce an estimate of the incident ionizing flux. Consider a column of length d along the line of sight to the star. The net hydrogen recombination rate within the column is

$$\Re = n_p n_e \alpha_B(T_e) d \text{ cm}^{-2} \text{ s}^{-1} , \quad (4)$$

where $\alpha_B(T_e)$ is the (case B) recombination coefficient. Interpolating over the temperature range expected for nebular gas, $\alpha_B(T_e) = 2.59 \times 10^{-13} t_4^{-0.833}$ cm^3 s^{-1}.

Assuming ionization balance, the net recombination rate in the column is equal to the rate of ionizations from stellar UV photons entering the column. The H-ionizing flux per unit area impinging on an ionized surface at a distance R from the central star is $Q_0/(4\pi R^2)$. For a radiation-bounded column of length $d \ll R$, this is equal to the number of ionizations per second $\Im$ within the column. With $\Re = \Im$, the H-ionizing flux of the central star is

$$\log Q_0 = 51.00 + \log [\mathrm{SB}(\mathrm{H}\alpha)(d/l) R(\mathrm{pc})^2] + g(t_4) + C(\mathrm{H}\alpha) \quad (5)$$

$$\geq 40.37 + \log [\mathrm{SB}(\mathrm{H}\alpha)(d/l)\theta(\mathrm{arcsec})^2] + 2 \log D(\mathrm{pc}) + g(t_4) + C(\mathrm{H}\alpha) , \quad (6)$$

where $g(t_4) = 0.150 \log t_4 + 0.0424/t_4$ and R and θ are respectively the true and projected distances between the star and structure. The second formula arises from the fact that $\theta \leq R/D$, where D is the distance to the nebula. If one determines a sufficiently accurate estimate of $\log Q_0$ for the ionizing star, one can in principle exploit this relation to determine the projection angle of the star-structure line of sight relative to the plane of the sky.

3. ESTIMATING THE IONIZING FLUX OF BD +60°2522

The distance to NGC 7635 was determined in Paper I to be 2400 pc; at that distance, 1″ translates to 1.16×10^{-2} pc. Our images contain two series of ionized knots, one to the west that falls within the bubble perimeter and another to the north outside it. The northern knots resemble pillars commonly seen in H II regions; the western knots, composed of two intersecting ridges, have been designated in the literature as "cometary" because of their resemblance in ground-based images. We will employ the method outlined above to estimate the total ionizing flux of the central star from the Hα image. As discussed in Paper I, the F656N filter admits a small fraction of the [N II] emission; the Hα surface brightnesses are thus measured from the F656 image corrected with the F658N image.

In Paper I, we also presented STIS spectra of the brightest of the western knots. Analysis of the line emission gives a T_e([N II]) of 7950 K. We will assume this temperature for all the knots in which we estimate n_p and $\log Q_0$; that is, $f(t_4) = 1.108$ and $g(t_4) = 0.038$.

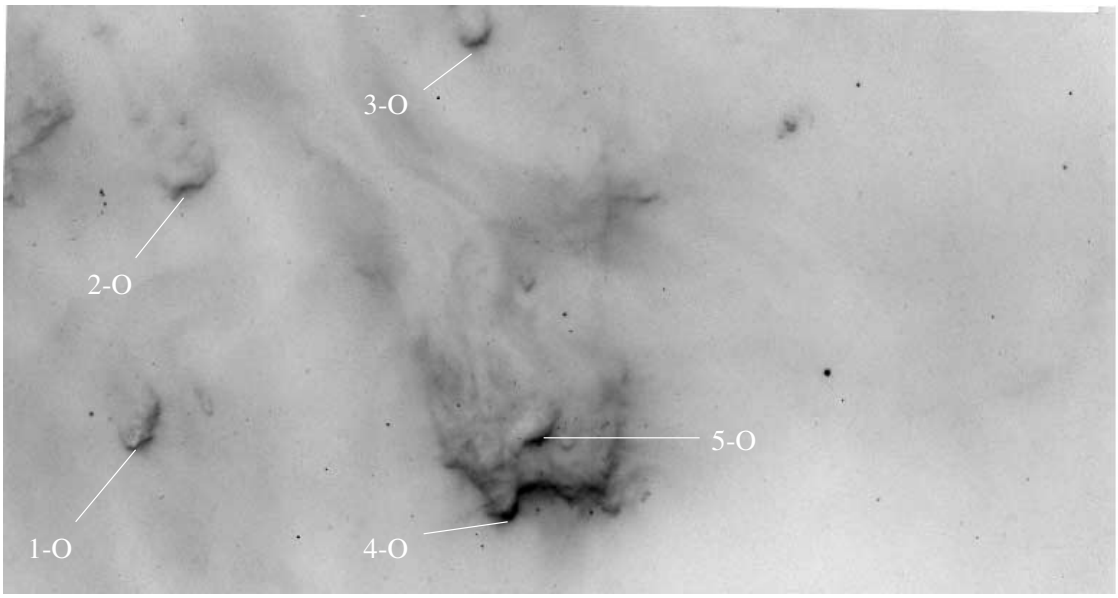

FIG. 1.—Positions chosen for analysis among the northern knot complex

TABLE 1
DATA FOR NORTHERN KNOTS

Position	SB(Hα)[a]	d/l (arcsec)	θ (arcsec)	n_H[b] (cm^{-3})	log Q_0
1-O.....	0.0023	0.3/0.8	114	3300	48.92
2-O.....	0.0023	0.4/1.2	127	2700	48.96
3-O.....	0.0023	0.4/1.0	131	2900	49.07
4-O.....	0.0046	0.4/1.2	100	3800	49.05
5-O.....	0.0029	0.6/1.1	104	3100	49.10

[a] In ergs cm^{-2} s^{-1} sr^{-1}.
[b] With 1.16×10^{-2} pc $arcsec^{-1}$.

3.1. *Northern Knots*

The knots to the north of the central star are outlined by bright ionized emission, suggesting that they lie approximately in the plane of the sky. Hence, using the angular separation of the knot and star should yield reasonably accurate estimates for Q_0. The degree of reddening can be assessed from the ratio of Hα and Hβ emission; bright areas of this region have $F(\mathrm{H}\alpha)/F(\mathrm{H}\beta) \simeq 6$. This corresponds to $C(\mathrm{H}\alpha) = 0.70$, using the reddening curve of Cardelli, Clayton, & Mathis (1989) with $R_V = 3.1$ and the expected ratio of 2.87.

Figure 1 indicates five positions chosen for analysis, on the basis of brightness and apparently simple geometries. Data for these positions and inferred values for n_H and log Q_0 are given in Table 1. The estimated H-ionizing flux of BD +60°2522 based on the northern knots is log $Q_0 = 49.02 \pm 0.10$, with the spread approximately equal to the composite errors of the data taken from the images.

3.2. *Western Knots*

Positions along the western knot complex can be divided into three groups: the closest condensation, a ridge that extends westward from the closest point, and a ridge that extends northward from the closest point. The ratio $F(\mathrm{H}\alpha)/F(\mathrm{H}\beta)$ in this region ranges from 6 to 8. Using the average value of 7 for all positions, this translates to $C(\mathrm{H}\alpha) = 0.85$. The positions chosen for analysis are indicated in Figure 2, and the results are presented in Table 2. For two of the positions (2-N and 3-N), there was an absence of curvature in the plane of the sky; for these positions, $l = d$ was assumed.

TABLE 2
DATA FOR WESTERN KNOTS

Position	SB(Hα)[a]	d/l (arcsec)	θ (arcsec)	n_H[b] (cm^{-3})	log Q_0
1-C.....	0.0360	0.4/0.5	20.5	19300	49.10
2-C.....	0.0330	0.4/0.7	21.5	15600	48.96
1-W.....	0.0120	1.0/1.8	25.5	5900	48.65
2-W.....	0.0230	0.7/1.4	39.5	9200	49.27
3-W.....	0.0032	0.3/1.0	47.0	4100	48.34
4-W.....	0.0040	0.3/1.1	60.0	4300	48.61
1-N	0.0110	0.3/1.0	23.0	7500	48.26
2-N	0.0043	0.4/0.4	24.0	7500	48.41
3-N	0.0023	0.4/0.4	29.0	5500	48.30
4-N	0.0015	0.5/0.5	30.5	3900	48.16

[a] In ergs cm^{-2} s^{-1} sr^{-1}.
[b] With 1.16×10^{-2} pc $arcsec^{-1}$.

The values of log Q_0 from the two positions in the closest condensation are consistent with that estimated from the northern knots. The estimate from the northern extent, however, disagrees by a factor of 4. This is most likely the result of projection effects, with the true distance from the star ~3 times larger than the projected distance. The results for the western ridge differ by a factor of 2. The exception is 2-W, which exceeds the value derived for the northern knots. These variations are likely the result of projection effects and absorption by significant amounts of photoevaporated material, with a relatively clean line of sight for 2-W.

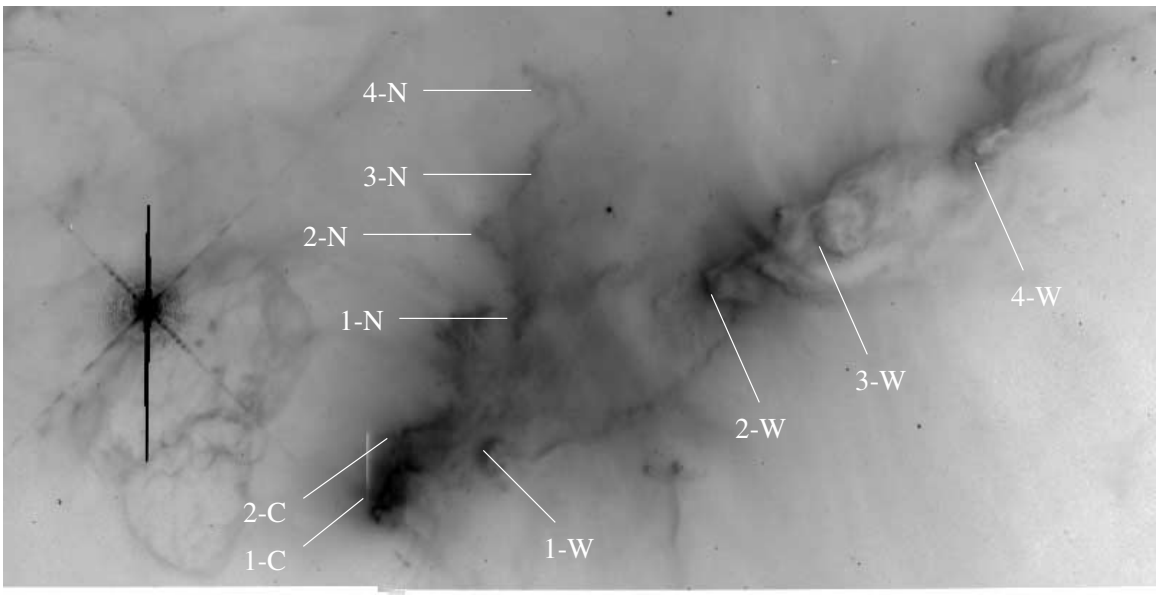

FIG. 2.—Positions chosen for analysis among the western knot complex

4. PHOTOEVAPORATIVE MODELS

The analysis above is useful as an estimate of the amount of ionizing flux from the central star but reveals nothing of the stellar temperature. It also says nothing of the chemical constituency of the nebular gas. By contrast, a spectral analysis of the sort presented in Paper I is useful for a compositional study but reflects the shape of the ionizing spectrum in only the coarsest sense. In addition, it enforces a number of simplifying assumptions about the distribution of nebular material that contradict the morphology seen in the images. We circumvent these shortcomings by using photoionization models with more realistic density distributions. These can then be directly compared with structures seen in our *Hubble Space Telescope* imagery of NGC 7635. We will again focus on the two series of knots north and west of BD $+60^{\circ}2522$.

4.1. *Spatial Profiles*

One knot in each of the two knot complexes was chosen for analysis, based on its brightness and simple geometry. The positions of the two profiles chosen for analysis are shown in Figure 3, with a width for the northern profile of 10 pixels, and for the western profile of 2 pixels. Spatial profiles of the line emission were extracted from the mosaicked filter images, with the conversion from data numbers to flux performed as outlined by Holtzman et al. (1995). Because of the 2×2 on-chip binning of the F487N images, its mosaic was resampled to match the spatial scale of the other images. To account for contamination of reflected stellar continuum, the spatial profiles from the F547M images were scaled by the relative widths of the individual filters and subtracted. The leak of Hα flux into the F658N filter and [N II] flux into the F656N filter were accounted for by subtracting 15% of the F658N profiles from those of the F656N filter and then subtracting 5% of the corrected F656N profiles from those of F658N. Finally, the amount of reddening was determined from the observed $F(\mathrm{H}\alpha)/F(\mathrm{H}\beta)$; no spatial variation could be detected beyond the noise level of either profile, so the amount of reddening was assessed but no correction was applied to the profiles. The final set of profiles for each knot were then ready for comparison.

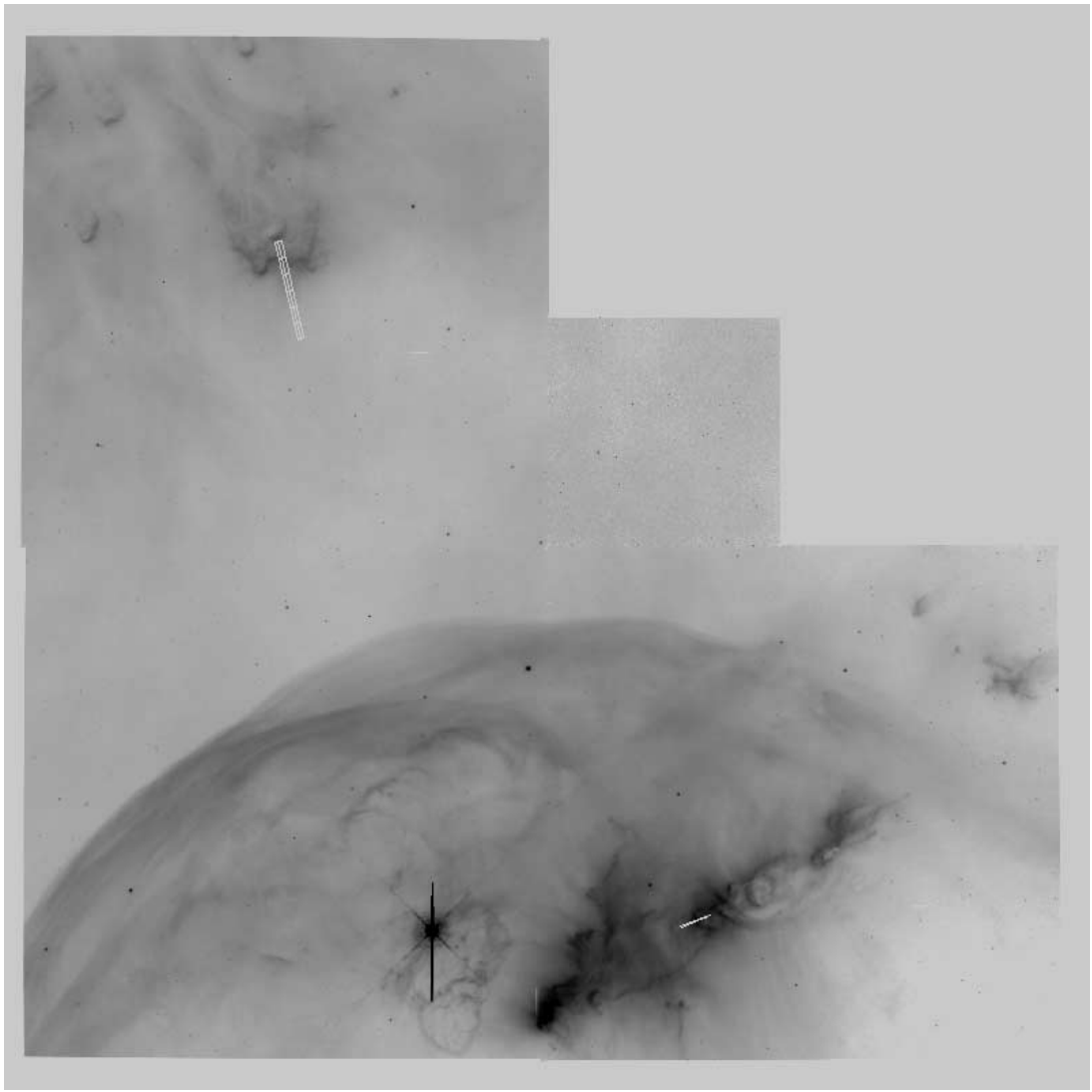

FIG. 3.—Positions of the spatial profiles extracted from the imagery, shown on the Hα mosaic. The northern and western profiles are averaged over slit widths of 10 and 2 pixels, respectively.

4.2. *Description of Photoevaporative Models*

To simulate a photoevaporating interface, a density profile of the model knots was given by

$$\rho(\boldsymbol{r}) = \rho(r_c) \exp\left[-(r + r_c)/h_c\right], \quad (7)$$

where $\rho(r_c)$ is the density at radius r_c and h_c is the scale height of gas in the ionized region. This corresponds to the photoevaporative models of Bertoldi & McKee (1990) for an isothermal cloud. Note that this density distribution and scale height need only be applicable within the ionized region of the cloud, as there was no attempt to treat the flow of neutral or ionized gas dynamically.

The models were placed at their respective projected distances from the central star, and the resulting models were calculated with the widely used photoionization code Cloudy 94.00 (Ferland et al. 1998). Because Cloudy is a one-dimensional code, further simplifications were required. Variation in the plane of the sky perpendicular to the line of sight to the star was suppressed. This effectively neglects the curvature of the knots in the plane of the sky, a reasonable assumption for sufficiently narrow profile extractions. The vector $\boldsymbol{r}$ was then decomposed into two components: x, along the direction toward the star, and y, perpendicular to the plane of the sky. The radial density profile was then replaced by a series of slabs of thickness $h_c/5$ centered at y-values from 0 to $+4h_c$ and exploiting the model symmetry to cover the $-y$ portion. Even with these simplifications, this model presents a more physically realistic picture of a photoevaporating region than is typically used when interpreting spectra.

The parameters of the Cloudy models were varied to maximize the agreement with the observed line emission profiles. Besides those used in the density distribution, other parameters of the fits include Q_0, the total H-ionizing flux required to ionize the on-axis density profile from $r_c + 4h_c$ to r_c; the shape of the ionizing continuum; and the elemental abundances of nitrogen, oxygen, and sulfur. The input stellar flux models were chosen from the suite of PHOENIX O star atmosphere models presented in Aufdenberg (2000) and provided to us by the author. The fundamental stellar parameters of these models (e.g., $T_{\rm eff}$, log g) were matched to those of Vacca, Garmany, & Shull (1996, hereafter VGS96), who calibrated these parameters as a function of stellar type. The abundances of all other elements were set to the Cloudy default values for an H II region, which are means of several observational results for the Orion Nebula.

4.3. *Model Results*

For each set of input parameters, the emissivity profiles of the 21 individual slabs were rebinned to a common spatial grid and integrated along y. The resulting one-dimensional emission profiles were convolved with a Gaussian of width similar to the WFPC2 point-spread function (approximately 0.5 pixels). The profiles were reddened to match the observed $F(\mathrm{H}\alpha)/F(\mathrm{H}\beta)$, using the curve of Cardelli et al. (1989) with $R_V = 3.1$. In addition to the relative spatial distribution of the line fluxes, the Hα emission peak was required to occur at the same distance as the (projected) distance in the Hα image.

The model parameters and input stellar spectrum were then varied iteratively for the northern knot model to maximize its agreement with the observations. In particular, the separation of the [O III] and Hα emission peaks is most sensitive to the effective temperature of the input stellar model. This best-fit model was found with a stellar spectrum of $T_{\rm eff} = 34{,}320$ K and log $Q_0 = 48.92$. Changing Q_0 by 0.01 dex results in noticeable changes to the model, so we claim a conservative uncertainty in our value of ± 0.02 dex. Because of its high density and proximity to the star, the western knot model is less sensitive to changes in Q_0 and $T_{\rm eff}$. The stellar input parameters were thus fixed to those of the northern knot model when constructing the best fit for the western knot, with the addition of an illumination angle of 10° relative to the normal of the ionized edge to match that seen in the image.

Visualizations of the best-fit models are shown in Figure 4. The extracted profile and best-fit model for the outer and inner positions are shown in Figures 5 and 6. The undulation in the profiles beyond the peak in the Hα emission are artifacts of the discrete slabs constituting the total profile. The best-fit parameters for the final models are shown in Table 3. The uniqueness and overall uncertainty in the model profiles are difficult to quantify, but a change in the total abundance of an element of ± 0.01 results in a noticeable shift in the output line emission. The quoted uncertainties are the scale factors required to shift the line emission from the given ion entirely above or below that observed.

The model sulfur abundances in the two knots agree within the stated error, whereas the difference in the nitrogen abundances exceeds it slightly. There is a large discrepancy, however, between the oxygen abundances of the two models, with that of the inner knot model 3 times lower than that of the outer knot model. It is clear from the observed Hα profile that the density in the northern knot model is too low at the [O III] emission peak. Correcting the factor of 2 difference in the observed and model Hα emission would roughly double the model [O III] emission [since $F([\mathrm{O\ III}]) \propto N(\mathrm{O}) n_e \propto N(\mathrm{O})/N(\mathrm{H}) n_p n_e$]. Thus, the oxygen abundance in the northern knot model may be overestimated by as much as a factor of 2. The fit to the western knot is of higher quality than that of the northern knot; however, the background subtracted from the [O III] was approximately equal to the peak value in the observed pro-

TABLE 3
PARAMETERS FOR BEST-FIT MODELS OF KNOTS IN NGC 7635

Model	$\rho(r_c)$ (cm^{-3})	r_c (cm)	h_c (cm)	O	S	N
Northern knot.....	1750	2.0×10^{17}	1.03×10^{17}	8.77	6.89	7.60
Western knot	6950	1.3×10^{17}	3.75×10^{16}	8.20	6.86	7.45

NOTE.—Abundances are given by number of element X, written as $12 + \log[\mathrm{X/H}]$.

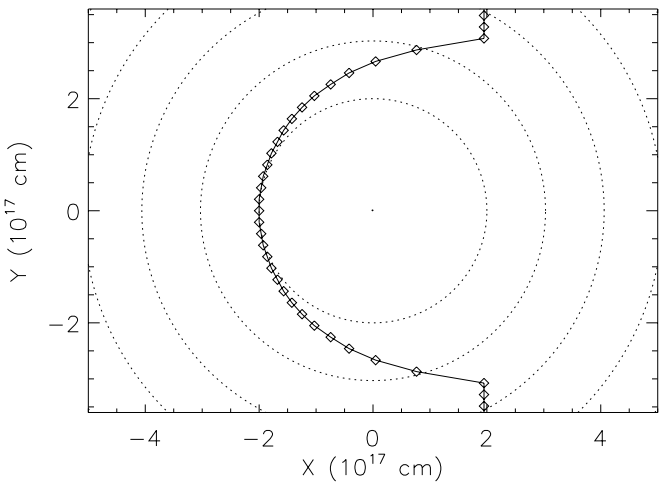

FIG. 4*a*

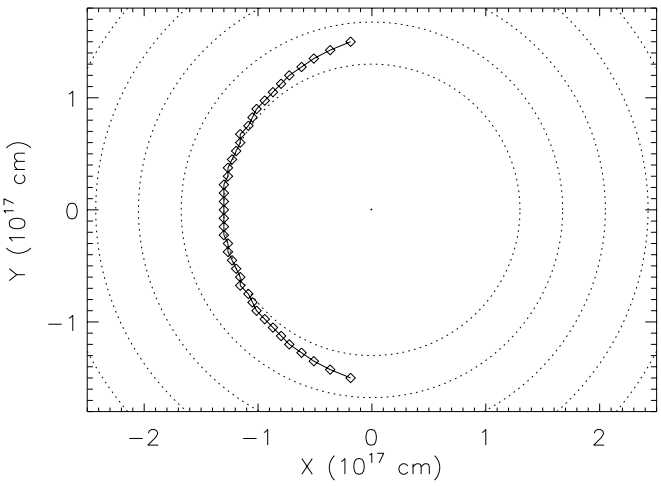

FIG. 4*b*

FIG. 4.—Two-dimensional representation of the (*a*) northern and (*b*) western knot models. The *x*-axis is along the direction to the star, with values increasing with increasing distance. The *y*-axis is aligned normal to the plane of the sky. The emission profile is created by integrating along *y*; the diamonds indicate the ionization edges (or outer radius) of the individual slabs. Contours of constant density are shown by dotted lines, centered on the peak model density and dropping successively by $1/e$ starting at $\rho = \rho(\mathbf{r}_c)$.

file. Oversubtraction could lead to an underestimate in the oxygen abundance by a factor of 2 as well. With this in mind, our results are insufficient to claim any differences in the elemental abundances between the two models.

4.4. *Spectral Analysis of Knot Models*

It is an interesting exercise to analyze the integrated emission-line strengths of the models as if they were observed spectra. Comparison between the input abundances and those derived from the "spectral" analysis allows us to assess the impact of the density distributions on the accuracy of results under the simplifying assumptions imposed by the standard methods of nebular abundance analysis. These assumptions include the distribution of ions within one of a few "ionization" zones and the use of empirical ionization correction factors ($i_{\rm CF}$) to convert from ionic to total elemental abundances.

To this end, the spatial profiles were integrated over emission lines of astrophysical interest and processed as were the spectra presented in Paper I. Here we follow the general prescription as outlined by Shaw & Dufour (1995), including the specific zone structure and weighting of each zone's density and temperature from diagnostic lines. Whenever

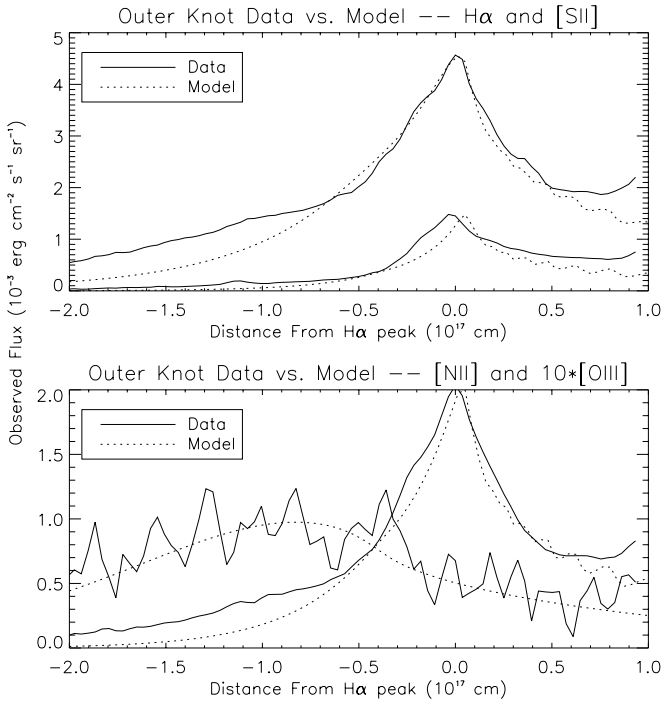

FIG. 5.—Emission-line profile of the northern knot, compared with the best-fit model.

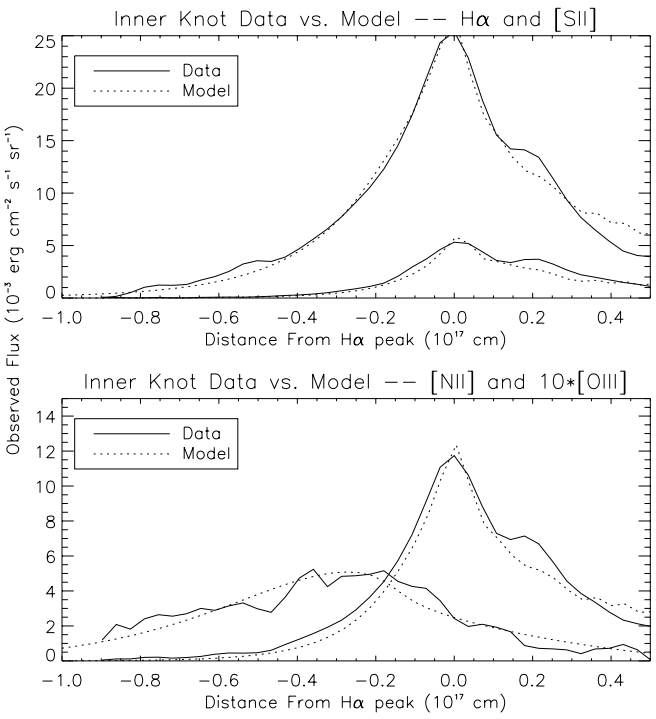

FIG. 6.—Same as Fig. 5, but for the western knot

TABLE 4
SPECTRALLY DERIVED IONIC ABUNDANCES FOR KNOT MODELS

Ion	Northern Knot Model	Western Knot Model
O^+	8.70	8.06
O^{++}	7.32	6.88
S^+	6.36	6.25
S^{++}	6.76	6.73
N^+	7.51	7.34
He^+	10.75	10.73
Cl^{++}	4.83	4.82
Ne^{++}	5.04	5.19
Ar^{++}	6.18	6.16

NOTE.—Abundances are given by number of ion X, written as $12 + \log [X/H^+]$.

possible, however, we use a given ion's density, temperature, or both to determine its abundance, instead of the weighted average of its zone. Particular attention was paid to matching the atomic data used in the analysis software to that used in Cloudy; test runs involving constant-density slabs show an agreement between the model and spectrally derived ionic abundances of 0.02 dex or better. Thus, we will assume that any deviations in the final elemental abundances are the cumulative result of the model density distribution and i_{CF} methodology.

The ionic abundances derived from the model spectra are given in Table 4. These are used in conjunction with commonly used i_{CF}'s to produce elemental abundances; the results are given in Table 5. The empirical i_{CF}'s for each element except argon were taken from Peimbert & Torres-Peimbert (1977), which was also the main source used to calculate the total abundances for NGC 7635 in Talent & Dufour (1979). The i_{CF} for argon was taken from Garnett et al. (1997). Note that the deviations for all elements except sulfur exceed the expected error of the method, with those for neon and argon especially high. The effect of structure on large and small scales on spectral analysis is underappreciated in the literature and will be the subject of a future paper (Moore, Hester, & Dufour 2002a).

5. IMPLICATIONS FOR BD +60°2522

The best-fit models employed a stellar model atmosphere with a T_{eff} of 34,320 K. According to VGS96, this corresponds to an O9 star. By contrast, the stellar types of BD +60°2522 in the literature range from O5 III to O7 III.

TABLE 5
INPUT VERSUS SPECTRALLY DERIVED ABUNDANCES FOR KNOT MODELS

Model	O	S	N	He	Cl	Ne	Ar
Northern knot:							
Input	8.77	6.89	7.60	10.98	5.00	7.78	6.48
Spectral ...	8.72	6.90	7.53	11.07	4.83	6.44	6.18
Western knot:							
Input	8.20	6.86	7.45	10.98	5.00	7.78	6.48
Spectral ...	8.09	6.86	7.36	11.02	4.82	6.40	6.16

NOTE.—Abundances are given by number of element X, written as $12 + \log [X/H]$.

Attempts to fit the observations with stellar models of the corresponding T_{eff} (>40,000 K) produced emission profiles with [O III] zones considerably larger and [N II] and [S II] zones noticeably smaller than observed. The magnitude of the effect of varying T_{eff} is demonstrated in Figure 7, which shows the northern knot model illuminated by $T_{eff} = 35{,}700$ K (O8.5 III), 34,320 K (O9 III), and 32,930 K (O9.5 III) stars of the same log Q_0. The shift in the [O III] morphology is noticeable even over these comparatively smaller differences in T_{eff}, making a reconciliation between our stellar model and the spectral types inferred from VGS96 unlikely.

The case for our model star is strengthened by predicting an apparent magnitude for the star. This is done by relating its absolute magnitude to its H-ionizing flux; that is, $M_V = -2.5 \log Q_0 + C(T_{eff})$, where $C(T_{eff})$ depends only on the shape of the spectrum and is derived directly from the tabulation of the available PHOENIX models of Aufdenberg (2000). For $T_{eff} = 34{,}320$ K, one obtains $C(T_{eff}) = 116.88$; for $T_{eff} = 42{,}640$ K (O6 III), $C(T_{eff}) = 118.12$.

The apparent magnitude of a model star is given by

$$m_V = -2.5[\log Q_0 - 2 \log D(\mathrm{pc})] + C(T_{eff}) + A_V - 5 . \quad (8)$$

Note that from equation (6) the dependence of m_V on the distance to the star drops out. Thus, our estimate of m_V depends only on the estimated Q_0, $C(T_{eff})$, and A_V.

The catalog of Humphreys (1978) quotes for BD +60°2522 $m_V = 8.67$, $B-V = +0.41$, and $A_V = 2.19$. Our

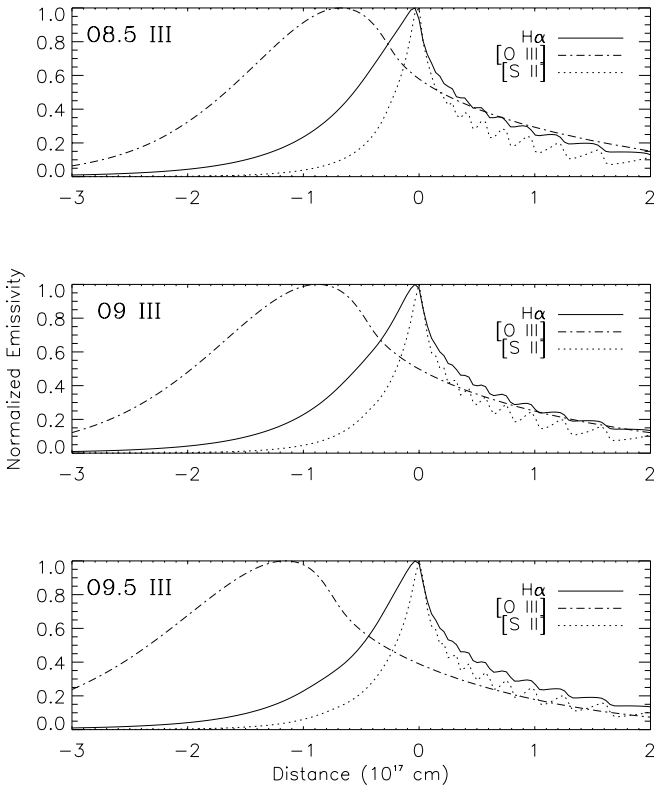

FIG. 7.—Comparison of models for the northern knot using stellar models with T_{eff} of 35,700 K (O8.5 III), 34,320 K (O9 III), and 32,930 K (O9.5 III). The shift in the position of the O III peak relative to that of Hα is noticeable even over this small range in stellar type. The model star of the middle model was the one used for the best-fit models presented in this paper.

value of $\log Q_0 = 49.02 \pm 0.10$ from the northern knots implies for the model O9 stellar spectrum $m_V = 8.42 \pm 0.25$, which marginally agrees with the observed value. The agreement is even more remarkable using the value of Q_0 from the emission-line models; $\log Q_0 = 48.92 \pm 0.02$ translates to $m_V = 8.67 \pm 0.05$. For consistency, one can determine A_V from the model atmosphere. For the model star, $B-V = -0.31$; combined with the observed value, $E(B-V) = 0.72$. For $R_V = 3.1$ this implies a visual extinction of $A_V = 2.23$ and $m_V = 8.71 \pm 0.05$, consistent with the observed value. A similar calculation for an O6 stellar model yields $m_V = 10.01$, seriously discrepant with observation; even with the largest estimate for $\log Q_0$ from the imagery, this star falls short of the apparent magnitude by more than 0.36 dex.

There have also been suggestions in the literature that the value of R_V toward S162 may significantly deviate from the Galactic average. For example, Rodríguez (1999) derives $R_V = 4.0$ and $R_V = 5.0$ for three positions within the western knot complex. We reject this assertion for the following reason: For $R_V = 4.0$, the $F(\mathrm{H}\alpha)/F(\mathrm{H}\beta)$ for the outer model requires an increase in $C(\mathrm{H}\alpha)$ from 0.76 to 0.92. This increases $\log Q_0$ to 49.08, and $m_V = 6.08 + A_V$. With $E(B-V) = 0.72$, the total visual extinction increases to $A_V = 2.88$, for an apparent magnitude of 8.96. Thus, to agree with observation the reddening law toward the star cannot be largely different in the V band from that of the average $R_V = 3.1$ curve.

It is unclear at this point how to resolve the difference between the model star and that inferred from its spectral type via VGS96. It is curious, however, that our model star closely fits the properties of the O9 star, with only a 0.05 dex difference in $\log Q_0$. One could invoke the presence of the strong stellar wind in the central star as the cause of the discrepancy. We have run test cases with a PHOENIX O6 model star that include the effects of wind blanketing; shifts in the emission-line morphology resembled more closely the models that used the wind-free O6 star than those that used the wind-free O9. The full impact of the temperature discrepancy for NGC 7635 can be demonstrated simply: a constant-density photoionization model using the hotter star underpredicts $N(\mathrm{O}^+)/N(\mathrm{O}^{++})$ by more than 1.0 dex compared with the observations of the western knots from Talent & Dufour (1979), Rodríguez (1999), or Paper I. We thus suggest that the results of VGS96 may be hampered by their reliance on static plane-parallel model atmospheres and should be reevaluated.

6. CONCLUSIONS

We have presented analysis and modeling of photoionized structures seen in NGC 7635. Of particular interest is the large effect of the density profile on the elemental abundances inferred from its spectra, following the traditional approach of interpreting nebular emission lines. Our analysis also has interesting implications for the total ionizing flux and effective temperature of the central star. Both point to a severe mismatch between its stellar type from spectra and its T_{eff} expected from the O star calibration of Vacca et al. (1996). The best-fit models used a spherical atmosphere from Aufdenberg (2000) with a T_{eff} of 34,000 K, at least 5000 K cooler than would be expected.

This work was supported by STScI grant GO-07515.03-96A at Arizona State University. B. D. M. would also like to thank J. P. Aufdenberg for supplying the stellar models and for helpful discussions on the implications of these results for the central star. This work was supported in part at all three institutions by AURA/STScI grant GO-7515. In addition, this work was supported at Arizona State University by NASA/JPL contracts 959289 and 959329 and Caltech contract PC 064528. B. D. M. acknowledges the support of AURA/STScI grant GO-08568.01-A to Rice University for postdoctoral support during the preparation of this paper. D. K. W. was also supported by NASA/URC NCCW-0085, NASA/MU-SPIN NCC 5-534, NASA/OSS NAG 5-10145, and with a travel grant from the South Carolina Space Grant Consortium.

REFERENCES

Aller, L. H. 1984, Physics of Thermal Gaseous Nebulae (Dordrecht: Reidel)
Aufdenberg, J. P. 2000, Ph.D. thesis, Arizona State Univ.
Bertoldi, F., & McKee, C. F. 1990, ApJ, 354, 529
Brocklehurst, M. 1971, MNRAS, 153, 471
Cardelli, J. A., Clayton, G. C., & Mathis, J. S. 1989, ApJ, 345, 245
Ferland, G. J., Korista, K. T., Verner, D. A., Ferguson, J. W., Kingdon, J. B., & Verner, E. M. 1998, PASP, 110, 761
Garnett, D. R., Shields, G. A., Skillman, E. D., Sagan, S. P., & Dufour, R. J. 1997, ApJ, 489, 63
Holtzman, J. A., Burrows, C. J., Casertano, S., Hester, J. J., Trauger, J. T., Watson, A. M., & Worthey, G. 1995, PASP, 107, 1065
Humphreys, R. M. 1978, ApJS, 38, 309
Moore, B. D., Hester, J. J., & Dufour, R. J. 2002a, in preparation
Moore, B. D., Walter, D. K., Hester, J. J., Scowen, P. A., Dufour, R. J., & Buckalew, B. A. 2002b, AJ, 124, 3313 (Paper I)
Peimbert, M., & Torres-Peimbert, S. 1977, MNRAS, 179, 217
Rodríguez, M. 1999, A&A, 351, 1075
Shaw, R. A., & Dufour, R. J. 1995, PASP, 107, 896
Talent, D. L., & Dufour, R. J. 1979, ApJ, 233, 888
Vacca, W. D., Garmany, C. D., & Shull, J. M. 1996, ApJ, 460, 914 (VGS96)